

Article

# Effects of the Particle Size of BaTiO<sub>3</sub> Fillers on Fabrication and Dielectric Properties of BaTiO<sub>3</sub>/Polymer/Al Films for Capacitor Energy-Storage Application

Lulu Gu <sup>1,2</sup>, Tao Li <sup>2</sup>, Yongjun Xu <sup>2</sup>, Chenghua Sun <sup>2</sup>, Zhenyu Yang <sup>2,\*</sup>, Deliang Zhu <sup>1,\*</sup> and Deliang Chen <sup>2,3,\*</sup> 

<sup>1</sup> College of Materials Science and Engineering, Shenzhen University, Shenzhen 518060, China; lulugu1130@163.com

<sup>2</sup> School of Materials Science and Engineering & School of Chemical Engineering and Energy Technology, Dongguan University of Technology, Dongguan 523808, China; ltnano@hotmail.com (T.L.); hnllxyj@dgut.edu.cn (Y.X.); chenghua.sun@monash.edu (C.S.)

<sup>3</sup> School of Materials Science and Engineering, Zhengzhou University, Zhengzhou 450001, China;

\* Correspondence: zyyang@dgut.edu.cn (Z.Y.); dlzhu@szu.edu.cn (D.Z.); dlchen@zzu.edu.cn (D.C.); Tel.: +86-371-67781046 (D.C.)

Received: 4 January 2019; Accepted: 25 January 2019; Published: 31 January 2019



**Abstract:** BaTiO<sub>3</sub>/polymer/Al (BPA) composite films for energy storage were fabricated by way of a roll coating and thermal curing process. The coating slurry consisted of silicon-containing heat-resistant resin (CYN-01) and BaTiO<sub>3</sub> particles with various particle sizes obtained from commercial BaTiO<sub>3</sub> powders processed at different durations of wet sand grinding in the presence of silane coupling agent (KH550), which not only improves the dielectric performance of the BPA films but also facilitates its production in a large scale. The major influence factors, such as the ratio between BaTiO<sub>3</sub> and resin and the size of BaTiO<sub>3</sub> particles, were investigated and their related mechanisms were discussed. The results show that modifying BaTiO<sub>3</sub> particles ( $D_{90} = 0.83 \mu\text{m}$ ) with the silane coupling agent of KH550 enhances the dielectric properties of the BPA films. The typical BPA films obtained exhibit a high dielectric constant of 32, a high break strength of 20.8 V/ $\mu\text{m}$  and a low dielectric loss of 0.014. The present work provides a simple and convenient way to prepare high-quality ceramic/polymer composite films for energy-storage application in a large scale.

**Keywords:** composite film; barium titanate; resin; silane coupling agent; dielectric property

## 1. Introduction

Capacitors with high energy and power densities are more and more indispensable in the present electronic information age [1]. Consumer electronic devices [2,3], smart and wearable electronics [4,5], aerospace industry [6], telecommunications equipment [7,8], the military industry [9] and the automobile industry [10,11], require high-performance capacitors and other energy-storage devices. To meet the demand for capacitors in the above applications, many capacitors with different types have been developed in recent years, including electrochemical capacitors (ECs) and dielectric capacitors. Electrochemical capacitors, including electric double layer capacitors (EDLCs) and pseudocapacitors (PCs), have attracted much attention owing to their high energy density, especially in terms of the electrochemical capacitors based on nanocarbon composites and 2D-materials [12,13]. The EDLCs based on carbon materials [14,15] and the PC based on metal oxides [16], metal oxides/graphene [17], MXenes [18] are achieved high energy density in recent reports. But the challenges in the power density

and stability of ECs still lie ahead. Recently, the capacitors based on high energy-storage-density dielectric materials (e.g., ceramics) have attracted increasing attention because their ultrahigh power density, excellent charge/discharge capability and long lifetime [19]. For energy-storage applications, the dielectric materials are expected to possess high dielectric constants and breakdown strengths, low dielectric losses, good temperature stability and high flexibility for easy manufacturing [20]. However, it is still a great challenge for materials scientists to achieve the high dielectric materials with the above excellent overall properties.

Composite dielectric films containing ferroelectric ceramic fillers and polymer matrixes have currently gained increasing attention, because these ceramics-based polymer composite films exhibit excellent dielectric properties and good flexibility as well as temperature stability [21]. For the ceramics-based polymer composite films, the properties of ceramic fillers, including their intrinsic dielectric properties, surface properties, size-distribution ranges, dimensions and morphologies, are the key factors that influence the performance of composite films and the resultant energy-storage devices [22]. Obviously, the intrinsic dielectric properties of the ceramic fillers have a direct impact on the dielectric performance of the composite films [23]. In addition, the size, morphology and surface characteristic of the fillers can affect the interfacial adhesion and dispersibility of the fillers in the polymer matrixes [24]. Therefore, the size-control and surface modification of ceramic fillers is vital to improve the dielectric performance of ceramics composite films.

The energy density ( $U_e$ ) of a dielectric material is defined as  $U_e = \int EdD$  and  $D = \epsilon E$ , where the  $D$ ,  $\epsilon$  and  $E$  are the electric displacement, dielectric permittivity and electric field, respectively [25]. In ceramics-based composite films, high- $\epsilon$  ceramic fillers, such as BaTiO<sub>3</sub> (BT), SrTiO<sub>3</sub>, BaSrTiO<sub>3</sub> and so on [26], are used to improve their dielectric permittivity and their breakdown strengths are usually modulated by adjusting the compatibility and monodispersity of the ceramic fillers in suitable polymer matrixes [27]. The aggregation of ceramic fillers and the defects existing at the interfaces between fillers and matrixes accelerate charges transmission, leading to a low breakdown strength.

To enhance dielectric properties and energy-storage performance, there have been many reports on the control of the size and morphology of ceramic fillers, the compatibility and dispersibility of the inorganic fillers in the polymer matrixes. Chen et al. [28] modified the BT nanoparticles using a rigid liquid-crystalline fluoro-polymer to improve the compatibility between BT nanoparticles and the poly(vinylidene fluoride-trifluoroethylene-chlorotrifluoroethylene) matrix and found that the breakdown strength and energy density of the composite film obtained at the optimal conditions reached 514 kV/mm and 16.2 J/cm<sup>3</sup>, respectively. Xie et al. [29] reported a nanocomposite film consisting of poly-(dopamine)-modified BaSrTiO<sub>3</sub> (PDA-modified BST) nanoparticles and poly(vinylidene fluoride) matrix and this film exhibited a dielectric constant of 35, a dielectric loss of 0.06 (at 100 Hz), a breakdown strength of 466 KV/mm and a high energy density of 11.0 J/cm<sup>3</sup>, indicating that the surface modification of BST with PDA remarkably enhances the compatibility of the two components and the structural homogeneity of the composite, which is the key to achieve high energy storage performance in composites films. Fu et al. [30] used BT nanorods (BTNRs) and BT nanoparticles (BTNPs) to fabricate BTNRs/PVDF and BTNPs/PVDF composite films and found that the BTNRs/PVDF film exhibits a higher dielectric permittivity than the BTNPs/PVDF due to the stronger internal electric field density distribution in the BTNRs/PVDF film. Zhu et al. [31] synthesized BT nanorods (BTNRs) by a microwave-assisted hydrothermal method and found that the BTNRs/epoxy composite film exhibits a high permittivity and good frequency stability. The above laboratory scale researches clearly indicate that the morphologies and surface modification of ceramic fillers highly influence the dielectric properties of the composite films and the energy-storage performance of the resultant capacitors. To achieve industrial scale applications, efficient and large-scale processes have to be developed to fabricate the ceramics/polymer films. Though the researches on the ceramics/polymer films for capacitor applications are multiple, the strategies suitable for industrial scale fabrication are still challengeable.

In this work, we make a preliminary feasibility investigation on the roll-to-roll fabrication of BT/polymer composite films on the basis of the industrial coating machine using an Al foil as the flexible substrate. The possible factors that influence dielectric properties of the BT/polymer/Al (BPA) composite films, including the size-distribution of pristine BT powders, ultrafine-treating parameters and the ratios ( $M_{BT}/M_{Polymer}$ ) of BT to polymer, are investigated systematically. The size and morphology control of the BT fillers is achieved by sand-milling and a silane coupling agent (i.e., KH550) is used to modify the BT surface and then enhance the compatibility between the BT fillers and polymer matrix. To imitate the industrial roll-to-roll coating process, we use a simple roll-coating method (see Figure 1) to fabricate BPA composite films, followed by a thermal curing. The typical BPA composite film obtained at the optimal conditions ( $M_{BT}/M_{Polymer} = 4$ ) exhibits a permittivity ( $\epsilon$ ), breakdown strength ( $E_b$ ) and loss ( $\tan\delta$ ) of 32, 20.8 V/ $\mu\text{m}$  and 0.014, respectively.

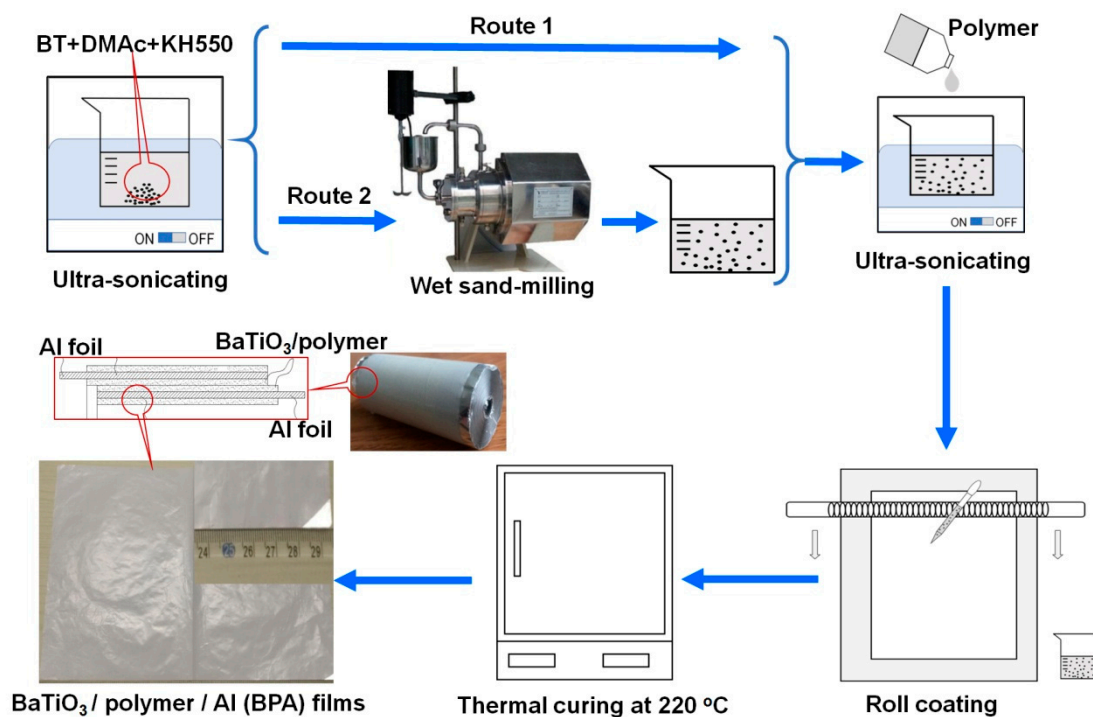


Figure 1. Schematic expression of the routes for the fabrication of BPA composite films.

## 2. Experimental

### 2.1. Chemicals and Setup

The polymer (ceramic glue), a silicon-containing heat-resistant resin, was purchased from the IPINRU Chen Yu Technology Co., Ltd (China, Product No. CYN-01 with a curing temperature of  $\sim 220$  °C). BaTiO<sub>3</sub> (BT, purity  $\geq 99.9\%$ ) powders were supplied by Zhejiang Jiukang Electric Co., Ltd. (Wenzhou, China). A silane coupling agent (KH550,  $\text{NH}_2\text{CH}_2\text{CH}_2\text{CH}_2\text{Si}(\text{OC}_2\text{H}_5)_3$ ) was purchased from Guangzhou Yuantai Synthetic Material Co., Ltd and dimethylacetamide (DMAc) was purchased from Guangzhou Jinhuada Chemical Reagent Co., Ltd. Al foils (thickness =  $\sim 12$   $\mu\text{m}$ , tensile strength  $\geq 180$  MPa, ductility  $\geq 15\%$ ) were purchased from Shenzhen Kejing Star Technology Co., Ltd. A sand miller (VB0.3Q, 0.3 mm of ZrO<sub>2</sub> beads) was purchased from Suzhou Weige Nano Technology Co., Ltd. A bar coater (XT-300CA) and coating rod (D10-OSP010-L0400) were purchased from Shijiazhuang Ospchina Machinery Technology Co., Ltd. A high temperature blast drying oven (DHG-9079A) was purchased from Shanghai Heheng Instrument Equipment Co., Ltd.

## 2.2. Fabrication of BaTiO<sub>3</sub>/Polymer/Al Films

The routes for the fabrication of BPA composite films are presented in Figure 1. Typically, the pristine BT powders and DMAc were mixed with a mass ratio of BT/DMAc = 2.2 and then the silane coupling agent (KH550) with an amount of 8 wt.% of BT powders was added to the above mixture, followed by an ultrasonic dispersion for 30 minutes. There were two routes to fabricate BPA films: Route 1 without sand-milling and Route 2 with sand-milling treatment.

In Route 1, after BT powders were uniformly dispersed in the DMAc/KH550 solution, a given amount of the binder polymer (CYN-01) was added to the DMAc/KH550/BT mixture and dispersed via ultrasonic treating for another 30 min to form a slurry containing BT and polymer. Then, a certain amount of the slurry was coated on an Al foil by a roll coater, followed by a curing treatment at 220 °C for 10 min and the BPA composite films were fabricated by Route 1. For Route 2, before the addition of the polymer (CYN-01), the DMAc/KH550/BT mixture was ultra-fined by the wet sand-milling for various times (1–60 min). The other processes for the fabrication of BPA composite films were similar to Route 1 (Figure 1).

## 2.3. Characterization and Dielectric Property Test

The X-ray diffraction (XRD) patterns of the BPA composite films and BT powders were recorded by a DX-2700BH X-ray diffractometer (Dandong Haoyuan, China) using Cu K $\alpha$  irradiation. The morphologies of the BPA composite films and BT powders were observed using a TM3030Plus electron microscope (Hitachi, Tokyo, Japan). The dielectric constant ( $\epsilon$ ) and loss ( $\tan\delta$ ) of the BPA films were measured using a high-precision high-voltage capacitor bridge (QS89, Shanghai Yanggao Capacitor Co., Ltd., Shanghai, China) and the dielectric performance test frequency was kept at 10 Hz. The breakdown strengths of the BPA films were measured using a withstand voltage tester (GY2670A, Guangzhou Zhizhibao Electronic Instrument Co., Ltd., Guangzhou, China). The particle sizes of the BT powders were measured using a laser particle size analyzer (LS-POP(VI), Omec Instruments Co., Ltd., Zhuhai, China). The film thickness of the BPA films was measured using a thousand fractions digital display of film sheet bench thickness gauge (CH-12.7-STSX, Shanghai Liuling Instrument Factory, Shanghai, China).

## 3. Results and Discussion

### 3.1. Fabrication of BPA Composite Films

The BT powders used for the fabrication of BPA composite films were synthesized via a solid reaction using BaCO<sub>3</sub> and TiO<sub>2</sub> as the reactants at 1300 °C. Figure 2 shows the XRD pattern, particle-size distribution and the typical SEM image of the pristine BT powders. As the XRD pattern in Figure 2a shows, the distinct peaks at  $2\theta = 22.12^\circ$ ,  $31.52^\circ$ ,  $38.81^\circ$ ,  $50.80^\circ$ ,  $56.10^\circ$  and  $65.76^\circ$  correspond to the (100), (110), (111), (210), (211) and (220) reflections of a cubic phase BT sample, respectively, according to the JCPDS card (no. 31–0174). The peak at around  $45^\circ$  consists of two sub-peaks at  $45.3^\circ$  and  $45.4^\circ$ , which can be attributed to (200) and (002) reflections of a tetragonal BT phase, respectively, according to the JCPDS card no. 05–0626 [32]. It may indicate that the BT sample may be a mixture of major cubic BT and minor tetragonal BT. Figure 2b shows the particle-size distribution plots of the pristine BT powders. The  $D_{90}$  of the pristine BT powders is about 2.08  $\mu\text{m}$  and its specific surface area is 5.52  $\text{m}^2/\text{g}$ . From the differential distribution curve, one can see that the particle size of the BT powders is concentrated at around 1.6  $\mu\text{m}$ . The SEM image of the pristine BT powders in Figure 2c shows that most of the BT particles are spherical but their sizes are not uniform. The sizes of most of the BT particles are less than 2  $\mu\text{m}$ , which agrees with the particles-size result analyzed using the laser size analyzer.

In the DMAc/KH550/BT suspension, KH550 acts as both a dispersing agent and a surface hydrophobic treatment agent to improve the dispersibility and compatibility of BT powders in the DMAc solution and polymer matrix. The adhesion between BT/polymer composites and Al foils

is excellent because of the coupling agent of KH550. The as-obtained BPA composite films after a curing treatment at 220 °C are gray, flexible and easy to be wound to form a cylindrical capacitor (see Figure 1).

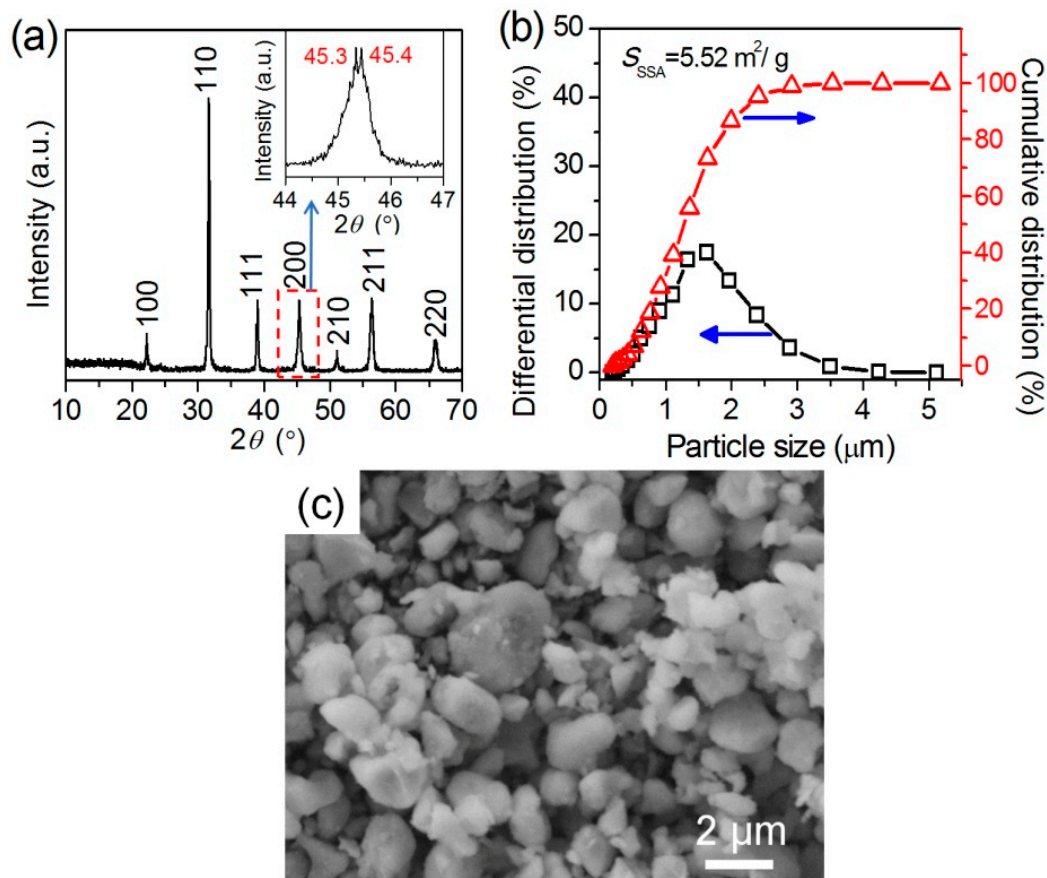


**Figure 2.** (a) X-ray diffraction (XRD) pattern, (b) particle-size distributions and (c) typical scanning electron microscopy (SEM) image of the pristine BT powders.

During the fabrication, the effects of surface modification (i.e., particle size) of BT powders by sand-milling treatment and mass ratios of BT to polymer on the dielectric properties of BPA composite films are systematically investigated via two routes with/without sand-milling treatment.

### 3.2. BaTiO<sub>3</sub>/Polymer/Al Composite Films with Pristine BaTiO<sub>3</sub> Powders

We firstly investigated the suitability of the pristine BT powders in the fabrication of composite BPA films via Route 1 (Figure 1). The pristine BT powders are of a  $D_{90}$  of 2.08  $\mu\text{m}$  with a specific surface area of 5.52  $\text{m}^2/\text{g}$ , as shown as Figure 2. The pristine BT powders are directly used to fabricate the BPA films with various  $M_{\text{BT}}/M_{\text{Polymer}}$  values using a small amount of KH550 as the coupling and dispersing agent.

The distribution of BT particles in the BPA films were observed using SEM and Figure 3 shows the typical SEM images of the BPA films prepared via Route 1 with various mass ratios of BT/polymer ( $M_{\text{BT}}/M_{\text{Polymer}}$ ). In the SEM images, the bright spots are BT particles and dark areas are polymer matrixes. As the value of  $M_{\text{BT}}/M_{\text{Polymer}}$  increases from 2 to 5, one can find that the BT particles become denser and denser. In Figure 3a, there are many areas without BT particles due to the low  $M_{\text{BT}}/M_{\text{Polymer}}$  value of 2. When  $M_{\text{BT}}/M_{\text{Polymer}} = 3$ , there are some small areas without BT particles as shown as Figure 3b. As the  $M_{\text{BT}}/M_{\text{Polymer}}$  ratio reaches 4, the as-obtained BPA film is uniformly distributed with BT particles in the polymer matrix (Figure 3c). Figure 3d shows a typical SEM image of the BPA film with  $M_{\text{BT}}/M_{\text{Polymer}} = 5$  and the BT particles are also uniformly distributed in the

BPA film. When comparing the two BPA films with  $M_{\text{BT}}/M_{\text{Polymer}}$  of 4 and 5, one can find that the particle density in the BPA films is similar but the edges of the BT particles in the BPA film with  $M_{\text{BT}}/M_{\text{Polymer}} = 5$  are clearer than those of the BPA film with  $M_{\text{BT}}/M_{\text{Polymer}} = 4$ . This point may be explained by the suitable interaction between BT powders and ceramic glue and more BT particles with a smaller amount of polymer lead to incomplete encapsulation. Therefore, the optimum ratio of  $M_{\text{BT}}/M_{\text{Polymer}}$  should be 4 for the formation of BPA films.

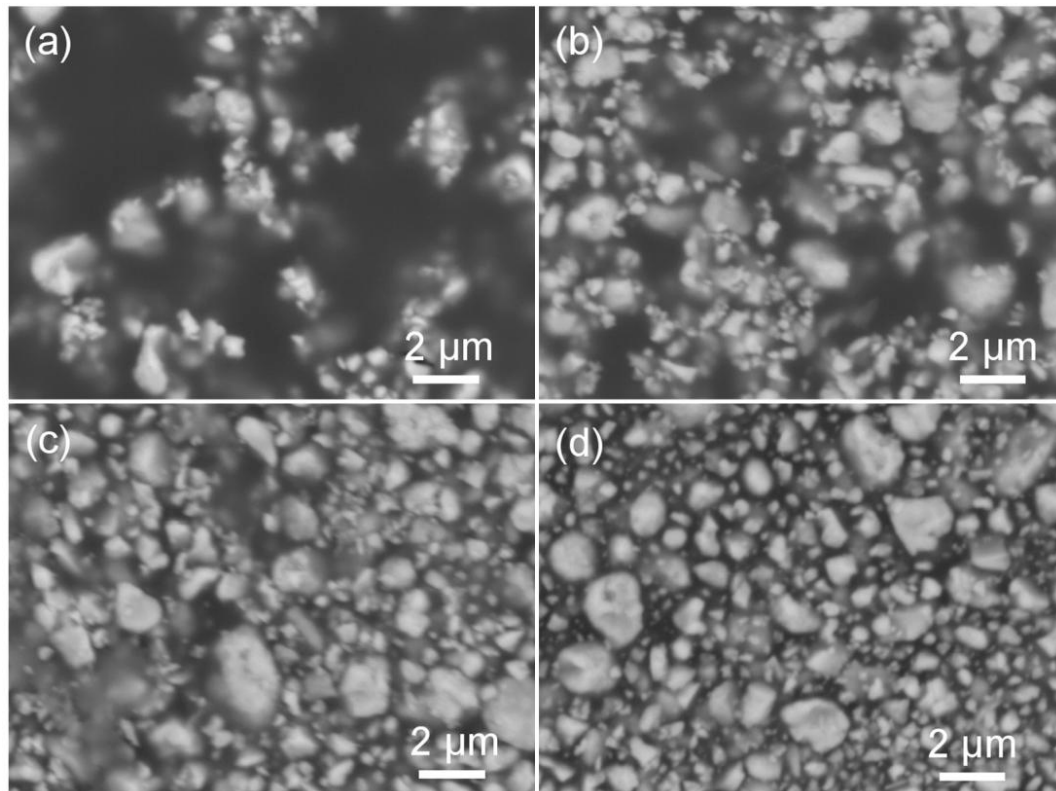


**Figure 3.** Typical SEM images of the BPA films fabricated via Route 1 with various BT/polymer mass ratios ( $M_{\text{BT}}/M_{\text{polymer}}$ ): (a) 2, (b) 3, (c) 4 and (d) 5.

Figure 4a shows the XRD patterns of the pristine BT powders, polymer/Al foil and BPA film ( $M_{\text{BT}}/M_{\text{polymer}} = 4$ ), determining the existence of the BT powders and Al foil. One can see that the BPA film (pattern C) is the superimposition of the pristine BT powders (pattern A) and Al foil (pattern B) and no other impurities can be found in the BPA film. The polymer (i.e., ceramic glue) is amorphous and no diffraction peaks belonging to polymer occur.

Figure 4b shows the dielectric constants and losses of the BPA films as a function of  $M_{\text{BT}}/M_{\text{polymer}}$ . One can see that as the  $M_{\text{BT}}/M_{\text{polymer}}$  ratio increases from 2 to 4, the dielectric constant and loss show a monotone increase. When  $M_{\text{BT}}/M_{\text{polymer}} = 4$ , the BPA film exhibits high dielectric constant of 8 and a dielectric loss ( $\tan\delta$ ) of 0.0062. But when the  $M_{\text{BT}}/M_{\text{polymer}}$  increases to 5, the dielectric constant and loss of the BPA film decrease sharply. This decrease may relate to the interaction and interface between BT powders and polymer species (refer to Figure 3). In general, in order to obtain a high dielectric constant, a common method is to increase the amount of ceramic fillers but at the same time the dielectric loss also increases obviously [33]. The possible reason should be that the higher filler amount in the BPA composite film, to some extent, reduces the bonding force between the BT powders and the electrode Al foil, as well as generates more pores and defects [34], leading to a larger dielectric loss. It should be noted that the dielectric constant of the BPA film is as low as 8 even at its optimum composition and we have to seek other means to improve the dielectric properties of the BPA films.

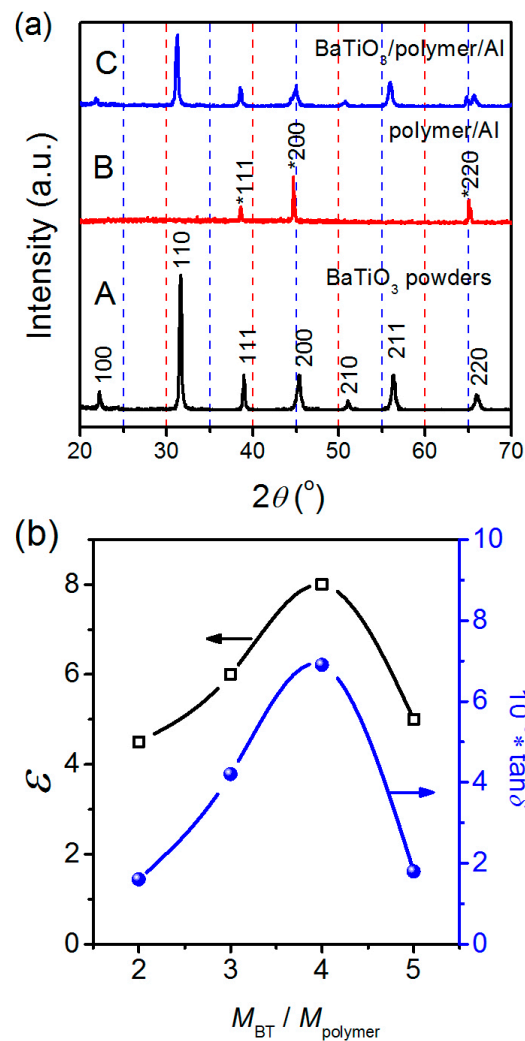


**Figure 4.** (a) Typical XRD patterns of the pristine BT powders, polymer/Al foil and BPA film ( $M_{BT}/M_{polymer} = 4$ ); (b) Plots of dielectric constant ( $\epsilon$ ) and dielectric loss ( $\tan\delta$ ) of BPA films obtained via Route 1 as a function of BT/polymer mass ratios ( $M_{BT}/M_{polymer}$ ).

### 3.3. BaTiO<sub>3</sub>/Polymer/Al Composite Films with Ultra-Fine BaTiO<sub>3</sub> Powders

To improve the dielectric properties of the BPA composite films, the pristine BT powders were ultra-fined for various times using a wet sand-milling method, because the sand-milling is an efficient method to produce superfine powders in an industrial scale. Figure 5 shows the cumulative and differential particle-size distribution plots of the BT powders obtained after sand-milling the pristine BT powders for different times ( $t = 1\sim 60$  min). From the cumulative particle-size distribution plots (Figure 5a), we can determine the  $D_{90}$  values of the BT powders after sand-milling for various times. When the sand-milling time is 1, 10, 20, 30, 40 and 60 min, the  $D_{90}$  values of the BT powders obtained is 1.90, 1.60, 1.27, 0.99, 0.83 and 0.61  $\mu\text{m}$ , respectively. Figure 5b shows the differential particle-size distribution plots of the BT powders obtained after sand-milling for various times. One can see that the particle-size distribution plots of the BT samples roughly accord with a normal distribution and that the smaller the  $D_{90}$  value is, the narrower the particle-size distribution range is. The regular particle-size change with the sand-milling time suggests that the wet sand-milling is an effective way to ultra-fine the pristine BT powders.

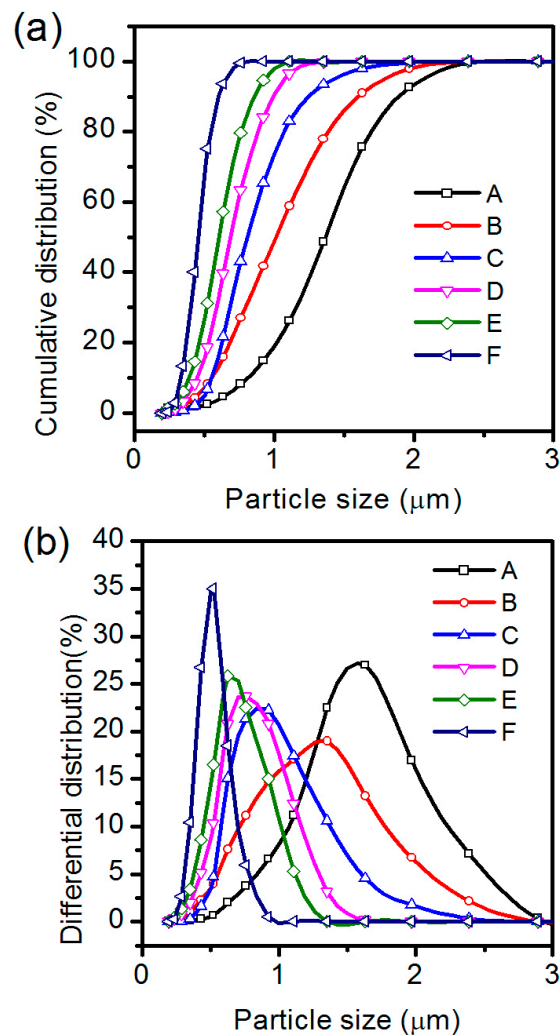


**Figure 5.** (a) Cumulative particle-size distribution curves and (b) differential particle-size distribution curves of the BT powders prepared by sand-milling the pristine BT sample for various times ( $t/\text{min}$ ): (A) 1 min, (B) 10 min, (C) 20 min, (D) 30 min, (E) 40 min and (F) 60 min.

The BT powders with various sand-milling times were used to fabricate BPA composite films via Route 2. Figure 6 shows the typical XRD patterns of the BPA films ( $M_{\text{BT}}/M_{\text{polymer}} = 4$ ) containing ultra-fine BT powders with various  $D_{90}$  values (0.61–1.90 μm). One can see that all the BPA films exhibit similar XRD peaks, belonging to the cubic BT phase and cubic Al phase (Figure 6a). The local enlarged XRD patterns at  $2\theta = 44\text{--}46^\circ$  are shown in Figure 6b. One can see that the (200) diffraction peak of Al becomes weaker and weaker (or even disappear) with the increase in the particle size ( $D_{90}$ ) of the BT powders from 0.61 to 1.9 μm. This phenomenon may be resulted from the gradual increase in the thickness of the BPA films and the Al foil cannot be detected by XRD in the BPA films with large-particle BT powders.

The morphologies and the distribution of the BT particles in the BPA composite films were further characterized using the SEM technique. Figure 7 shows the typical SEM images of the BPA films ( $M_{\text{BT}}/M_{\text{polymer}} = 4$ ) containing the BT powders with various particle sizes ( $D_{90} = 1.9, 1.6, 1.27, 0.99, 0.83$  and  $0.61$  μm). The insets of the SEM images are the corresponding local high-magnification SEM images. There are many large holes with a diameter of  $2 \sim 10$  μm in the BPA composite films, when the particle size ( $D_{90}$ ) of the BT powders used is larger than 1.0 μm (e.g., 1.9, 1.6 and 1.27 μm for Figure 7a–c, respectively). The larger voids and openings occur with larger BT particles in the BPA films (Figure 7a–c). As Figure 7d,e shows, when the particle sizes ( $D_{90}$ ) of the BT powders are

smaller than 1.0  $\mu\text{m}$ , for example, 0.99 and 0.83  $\mu\text{m}$ , the as-obtained BPA films become denser and more uniform. The holes gradually dwindle and even disappear and a dense and smooth BPA film (Figure 7e) is achieved when the  $D_{90}$  of the BT powder is 0.83  $\mu\text{m}$ . However, when the size ( $D_{90}$ ) of the BT fillers decreases to 0.61  $\mu\text{m}$ , some cracks occur in the BPA film, as shown as Figure 7f. These cracks in Figure 7f may be resulted from the aggregation of small BT powders in the BT/polymer composite. The other possible reason may be the unsuitable ratio of BT to polymer and smaller BT powders require a larger amount of polymer to form a uniform and fully infiltrated slurry.

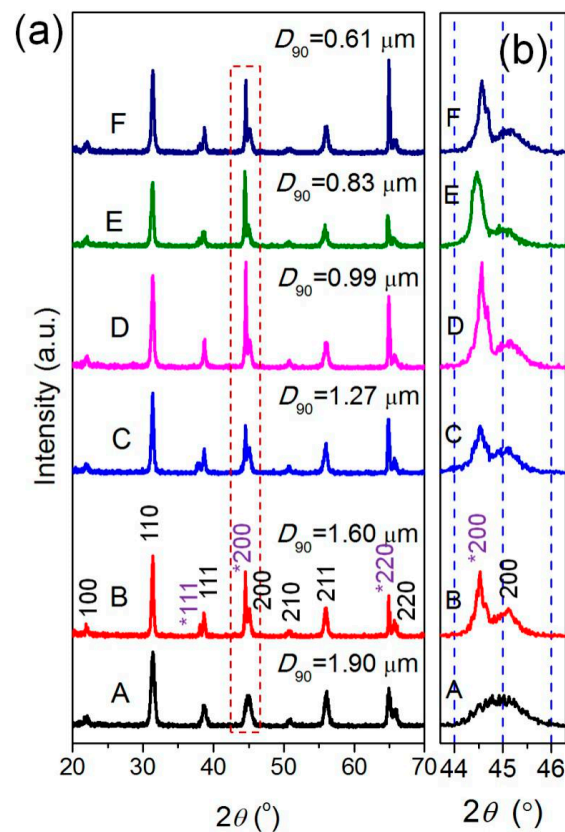


**Figure 6.** (a) XRD patterns of the BPA films obtained via Route 2 using BT powders with various particle sizes as the functional inorganic filler ( $M_{\text{BT}}/M_{\text{polymer}} = 4$ ); (b) the partial enlarged XRD patterns in the  $2\theta$  range of 45–46°.

When comparing with the BPA film ( $M_{\text{BT}}/M_{\text{polymer}} = 4$ ) fabricated via Route 1 (Figure 3c), one can see that the BPA films fabricated via Route 2 exhibit smoother and denser morphologies than those of the BPA films fabricated via Route 1, especially the BPA film filled with BT nanoparticles with  $D_{90} = 0.83 \mu\text{m}$  (Figure 7e). The results indicate that the wet sand-milling is an effective way to reduce the sizes of the BT particles and narrow their particle-size distribution, which is important to achieve a smooth and dense BPA film. According to Figures 6 and 7, the suitable BT size (e.g., 0.83  $\mu\text{m}$ ) is the key factor to form a dense and smooth BPA film.

The dielectric properties of the BPA films containing BT powders with various particle sizes are shown in Figure 8. Figure 8a shows the change of the dielectric constant and loss as a function of the BT particle size ( $D_{90}$ ). One can see that the BPA film containing the BT powders with a  $D_{90}$  of 0.83  $\mu\text{m}$  exhibits the highest permittivity of 32 and the other BPA films with larger or smaller  $D_{90}$  values show lower permittivity. The dielectric loss ( $\tan\delta$ ) shows a change trend similar to their permittivity. For the BPA film with  $D_{90} = 0.83 \mu\text{m}$ , its  $\tan\delta$  is about 0.014. The change of the breakdown strength and film thickness versus  $D_{90}$  of BT powders is shown in Figure 8b. When the BT particle size increases from 0.61 to 1.27  $\mu\text{m}$ , the thickness of the BPA film is kept at about 5  $\mu\text{m}$  and its breakdown strength is

slightly enhanced from 18 to 21 V/ $\mu\text{m}$ . When the size of BT particles increases from 1.27 to 1.9  $\mu\text{m}$ , the as-obtained BPA film becomes thicker and thicker, increasing rapidly from 5 to 10  $\mu\text{m}$  in thickness; whereas, its breakdown strength sharply drops from 21 to 5 V/ $\mu\text{m}$ . As Figure 8a,b shows, the BPA composite film with BT of  $D_{90} = 0.83 \mu\text{m}$  exhibits the largest permittivity of 32 and the BPA composite film with BT of  $D_{90} = 1.27 \mu\text{m}$  has the highest breakdown strength of 21 V/ $\mu\text{m}$ . When comparing Figure 8 with Figure 4, we find that the dielectric properties of the BPA films fabricated via Route 2 are obviously higher than those of the BPA films fabricated via Route 1, indicating the wet sand-milling is a crucial strategy to improve the dielectric performance of the BPA films due to the more uniform and dense distribution of BT powders.

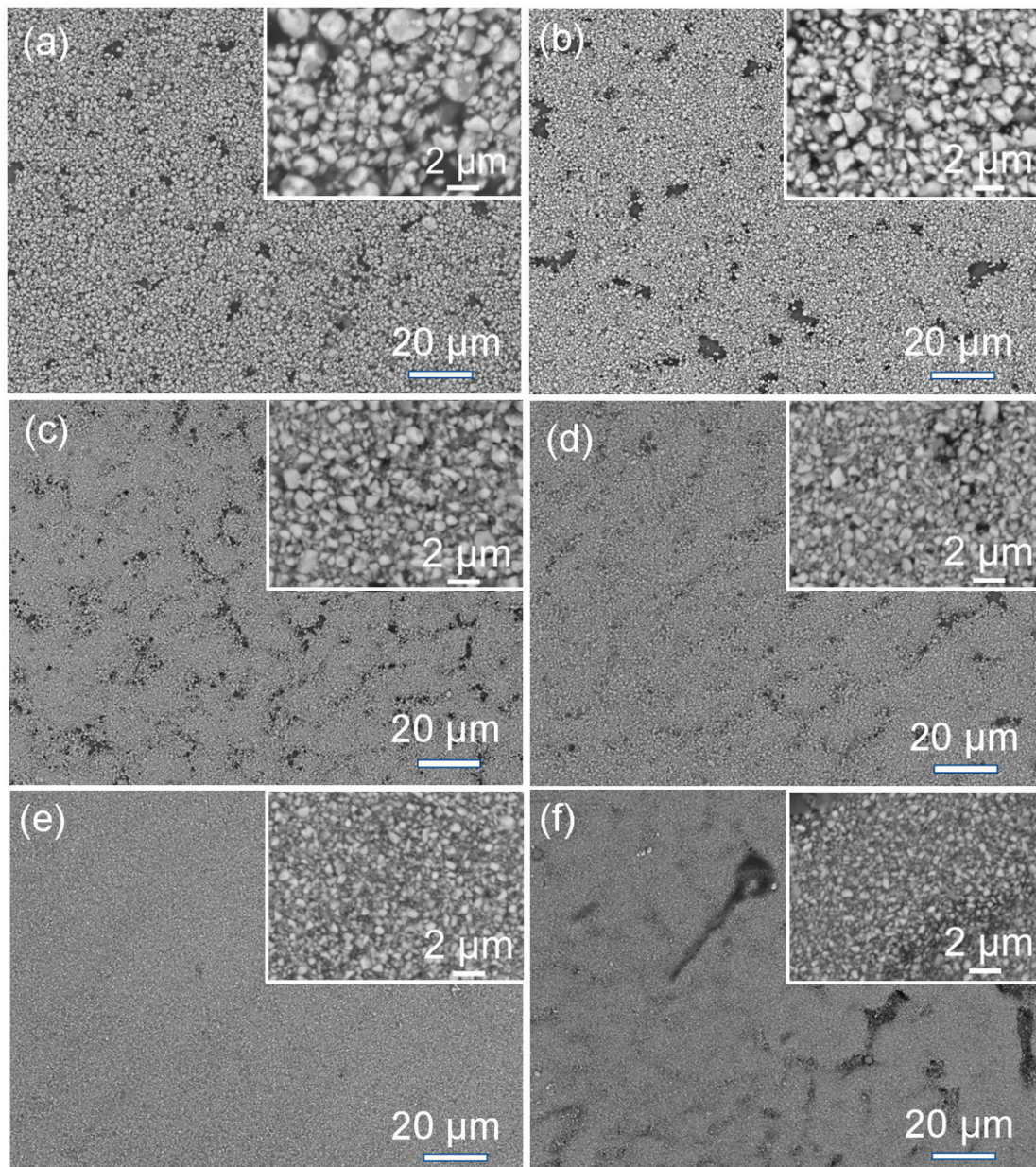


**Figure 7.** SEM images of the BPA films obtained via Route 2 using BT powders with various particle sizes as the functional inorganic filler ( $M_{\text{BT}}/M_{\text{polymer}} = 4$ ): (a)  $D_{90} = 1.9 \mu\text{m}$ , (b)  $D_{90} = 1.6 \mu\text{m}$ , (c)  $D_{90} = 1.27 \mu\text{m}$ , (d)  $D_{90} = 0.99 \mu\text{m}$ , (e)  $D_{90} = 0.83 \mu\text{m}$  and (f)  $D_{90} = 0.61 \mu\text{m}$ .

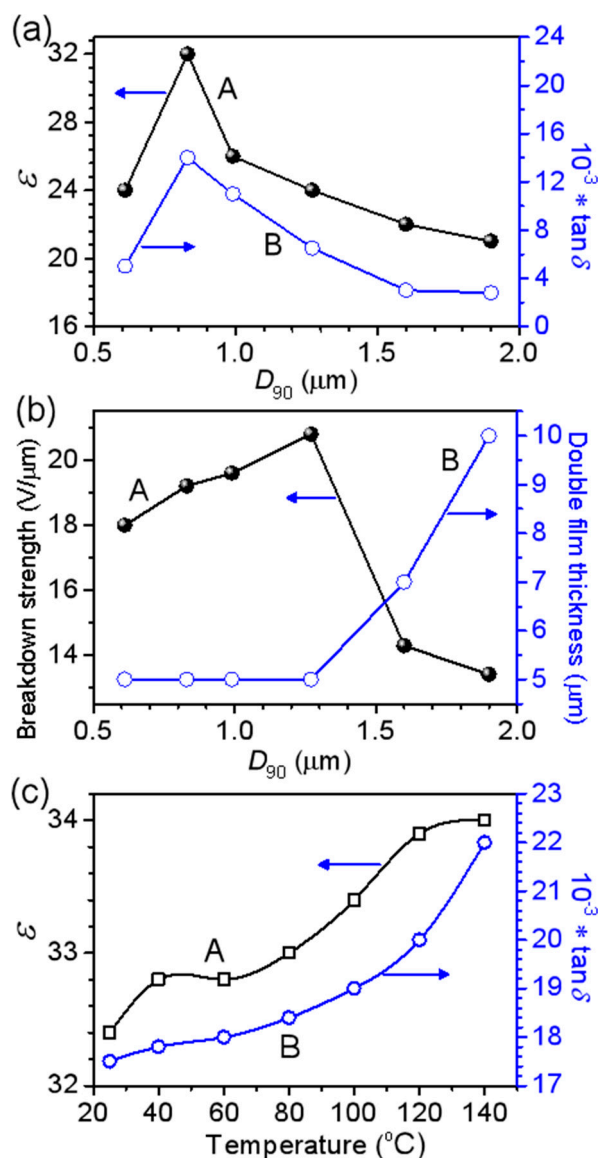


**Figure 8.** (a) Dielectric constant and loss of the BPA films obtained via Route 2 as a function of BT particle size ( $M_{\text{BT}}/M_{\text{polymer}} = 4$ ); (b) Breakdown strength and film double layer thickness of the BPA films as a function of BT particle size ( $M_{\text{BT}}/M_{\text{polymer}} = 4$ ); (c) Dielectric constant and loss of the BPA films obtained via Route 2 as a function of testing temperature ( $M_{\text{BT}}/M_{\text{polymer}} = 4$ ,  $D_{90} = 0.83 \mu\text{m}$ ).

Table 1 compares the dielectric properties of some ceramic/polymer composite films published recently. One can find that the BPA film prepared by the simple roll-coating method in this work shows good comprehensive dielectric properties (i.e., high dielectric constant and low dielectric loss). The high dielectric performance of the BPA films should be attributed to the dense and uniform arrangement of the BT particles, resulting from the fine BT particles with a narrow size distribution and the high compatibility between BT particles and polymer matrix. The sizes of BT particles prepared by wet sand grinding are more uniform than those obtained via other methods in previous works reported. On the other hand, the BT particles in the special resin CYN-01, produced by IPINRU Chen Yu Technology Co., Ltd. (Shenzhen, China), exhibits more compatible than those in PVDF. So, the dielectric performance of BPA film in this work is better than the others in previous works.

**Table 1.** Comparisons of dielectric constant, dielectric loss and breakdown strength of the composites containing BT particles.

Fillers	Polymer Matrix	Dielectric Constant	Dielectric Loss	Breakdown Strength	Ref.
BT microparticles	Resin	32	0.014	20.8 V/ $\mu$ m	This work
BT nanoparticles (60 nm)	In suit prepared polyimide	3.85	0.0024	334.26 kV/mm	[35]
PDA coated BT nanoparticles (100 nm)/BN nanosheets	Poly(vinylidene fluoride-chlorotrifluoroethylene)	11.7	0.10	425 MV/m	[36]
PVP coated BT nanoparticles (100 nm)	Poly(vinylidene fluoride)	80.4	0.085	240 kV/mm	[37]
BT@Al <sub>2</sub> O <sub>3</sub> nanoparticles (150 nm)	Poly(vinylidene fluoride)	17.5	0.02	312 kV/mm	[38]
Sphere-like TiO <sub>2</sub> nanowire clusters	Poly(vinylidene fluoride-co-hexafluoropylene)	11.9	0.048	160 kV/mm	[39]
Dopamine modified urchin-like hierarchical structure of BT particles @ TiO <sub>2</sub> nanowires	Poly(vinylidene fluoride-co-hexafluoropylene)	14.7	0.0037	240 kV/mm	[40]
Dopamine-coated BT@SiO <sub>2</sub> nanofiber	In suit prepared polyimide	5.05	0.0225	346 kV/mm	[41]
Ethylene propylene diene monomer coated BT nanoparticles (<100 nm)	Polypropylene	5.8	/	370 MV/m	[42]
CaCu <sub>3</sub> Ti <sub>4</sub> O <sub>12</sub> @TiO <sub>2</sub> nanofibers	In suit prepared polyimide	5.85	0.025	236 kV/mm	[43]
BT modified with 2-phosphonobutane-1,2,4-tricarboxylic acid	In suit prepared polyimide	23.5	0.00942	80 MV/m	[44]
BT/TH-615 acrylic-acrylate-amide copolymer	In suit prepared polyimide	20.3	0.00571	73 MV/m	[44]

Figure 8c shows the change in the dielectric constant and loss of the BPA film as a function of testing temperature ( $M_{BT}/M_{polymer} = 4$ ,  $D_{90} = 0.83 \mu\text{m}$ ). One can see that the BPA film shows stable dielectric properties in different test temperature and the dielectric constant and loss exhibit little fluctuation when the test temperature increases from 20 °C to 140 °C.

Taking Figures 7 and 8 into account, the particle size and distribution of BT powders have a tight effect on the dielectric properties of the corresponding BPA films obtained via Route 2. The BT powders with a  $D_{90}$  of 0.83  $\mu\text{m}$  obtained by wet sand-grinding for 40 min exhibit the highest dielectric properties in the present test conditions. These results are helpful in the fabrication of high-quality energy-storage devices on the bases of BT ceramic powders.

#### 4. Conclusions

In summary, a simple roll-coating and thermal curing process has been developed to fabricate BT/polymer composite films on Al foils for energy-storage capacitor applications. The particle sizes of the BT powders are conveniently modulated by the wet sand-milling treatment and the particle sizes of the BT powders have obvious effects on the dielectric properties of the as-obtained BPA composite films. The dielectric constant, break strength and dielectric loss of the BPA films can be efficiently regulated by the BT fillers with various particle sizes ( $D_{90}$ ). Under the optimal conditions, the BPA film containing BT with  $D_{90} = 0.83 \mu\text{m}$  exhibits a high dielectric constant of 32, a high break strength of 20.8 V/ $\mu\text{m}$  and a low dielectric loss of 0.014, being close to or beyond the results reported recently. This work provides a simple but industrial strategy to fabricate ceramic/polymer composite films for energy-storage capacitor applications.

**Author Contributions:** Conceptualization, D.C.; Methodology, L.G. and T.L.; Investigation, L.G., T.L. and D.C.; Resources, Y.X.; Data Curation, D.C. and Z.Y.; Writing-Original Draft Preparation, L.G. and D.C.; Writing-Review & Editing, C.S., Z.Y., D.Z. and D.C.; Supervision, D.C.

**Funding:** This research was funded by the National Natural Science Foundation of China [grant number 51574205]; the National Natural Science Foundation of Guangdong Province [grant number 2018B030311022]; Guangdong Innovation Research Team for Higher Education [grant number 2017KCXTD030]; High-level Talents Project of Dongguan University of Technology [grant number KCYKYQD2017017]; the Engineering Research Center of None-Food Biomass Efficient Pyrolysis & Utilization Technology of Guangdong Higher Education Institutes [grant number 2016GCZX009]; and Program from Dongguan University of Technology [grant number G200906-17].

**Acknowledgments:** The authors thank Zhejiang Jiukang Electric Co. LTD for partly providing experimental support and Junfeng Qiu, Shuyu Wang, Changsheng Zhou and Guizhong Huang for their help with the film preparation and the dielectric property test.

**Conflicts of Interest:** The authors declare no conflict of interest.

#### References

1. Shin, D.; Kwon, C.H.; Ko, Y.B.; Lee, S.W.; Lee, B.; Cho, J. Stitchable supercapacitors with high energy density and high rate capability using metal nanoparticle-assembled cotton threads. *J. Mater. Chem. A* **2018**, *6*, 20421–20432. [[CrossRef](#)]
2. Pourmousavian, N.; Kuo, F.W.; Siriburanon, T.; Babaic, M.; Staszewski, R.B. A 0.5 V 1.6 mW 2.4 GHz fractional-N all-digital PLL for bluetooth LE with PVT-insensitive TDC using switched-capacitor doubler in 28 nm CMOS. *IEEE J. Solid State Circuits* **2018**, *53*, 2572–2583. [[CrossRef](#)]
3. Hu, C.; Chen, M.; Li, H.; Zhang, Z.; Jiao, Y.; Shao, H. An accurate on-site calibration system for electronic voltage transformers using a standard capacitor. *Meas. Sci. Technol.* **2018**, *29*, 055901. [[CrossRef](#)]
4. Dubal, D.P.; Chodankar, N.R.; Kim, D.H.; Pedro, G.R. Towards flexible solid-state supercapacitors for smart and wearable electronics. *Chem. Soc. Rev.* **2018**, *47*, 2065–2129. [[CrossRef](#)] [[PubMed](#)]
5. Li, J.; Jiang, Q.; Yuan, N.; Tang, J. A review on flexible and transparent energy storage system. *Materials* **2018**, *11*, 2280. [[CrossRef](#)] [[PubMed](#)]
6. Ho, J.S.; Greenbaum, S.G. Polymer capacitor dielectrics for high temperature applications. *ACS Appl. Mater. Interfaces* **2018**, *10*, 29189–29218. [[CrossRef](#)] [[PubMed](#)]

7. Chen, G.; Peng, H.; Zeng, R.; Hu, Y.; Ni, K. A fundamental frequency sorting algorithm for capacitor voltage balance of modular multilevel converter with low-frequency carrier phase shift modulation. *IEEE J. Em. Sel. Top. Power Electron.* **2018**, *6*, 1595–1604. [[CrossRef](#)]
8. Araga, Y.; Nagata, M.; Miura, N.; Lkeda, H.; Kikuchi, K. Superior decoupling capacitor for three-dimensional LSI with ultrawide communication bus. *Jpn. J. Appl. Phys.* **2017**, *56*, 04CC05. [[CrossRef](#)]
9. Schunemann, B.; Schael, U.; Rauer, G.; Wickert, M.; Cunrath, R.; Nau, S. Rapid recharging power supply for multiple-hit electrical armor. In Proceedings of the 17th International Symposium on Electromagnetic Launch Technology, La Jolla, CA, USA, 7–11 July 2014; pp. 1–6.
10. Rezzak, D.; Boudjerda, N. Management and control strategy of a hybrid energy source fuel cell/supercapacitor in electric vehicles. *Int. Trans. Electr. Energy Syst.* **2017**, *27*, e2308. [[CrossRef](#)]
11. Lee, S.; Kim, J. Implementation methodology of powertrain for series-hybrid military vehicles applications equipped with hybrid energy storage. *Energy* **2017**, *120*, 229–240. [[CrossRef](#)]
12. Borenstein, A.; Hanna, O.; Attias, R.; Luski, S.; Brousse, T.; Aurbach, D. Carbon-based composite materials for supercapacitor electrodes: A review. *J. Mater. Chem. A* **2017**, *5*, 12653–12672. [[CrossRef](#)]
13. Khan, A.H.; Ghosh, S.; Pradhan, B.; Dalui, A.; Shrestha, L.K.; Acharya, S.; Ariga, K. Two-dimensional (2D) nanomaterials towards electrochemical nanoarchitectonics in energy-related applications. *Bull. Chem. Soc. Jpn.* **2017**, *90*, 627–648. [[CrossRef](#)]
14. Wang, Q.; Yan, J.; Fan, Z. Carbon materials for high volumetric performance supercapacitors: Design, progress, challenges and opportunities. *Energy Environ. Sci.* **2016**, *9*, 729–762. [[CrossRef](#)]
15. Genc, R.; Alas, M.O.; Harputlu, E.; Repp, S.; Kremer, N.; Castellano, M.; Colak, S.G.; Ocakoglu, K.; Erdem, E. High-capacitance hybrid supercapacitor based on multi-colored fluorescent carbon-dots. *Sci. Rep.* **2017**, *7*, 11222. [[CrossRef](#)] [[PubMed](#)]
16. Repp, S.; Harputlu, E.; Gurgun, S.; Castellano, M.; Kremer, N.; Pompe, N.; Woerner, J.; Hoffmann, A.; Thomann, R.; Emen, F.M.; Weber, S.; Ocakoglu, K.; Erdem, E. Synergetic effects of Fe<sup>3+</sup> doped spinel Li<sub>4</sub>Ti<sub>5</sub>O<sub>12</sub> nanoparticles on reduced graphene oxide for high surface electrode hybrid supercapacitors. *Nanoscale* **2018**, *10*, 1877–1884. [[CrossRef](#)]
17. Sengottaiyan, C.; Jayavel, R.; Bairi, P.; Shrestha, R.G.; Ariga, K.; Shrestha, L.K. Cobalt oxide/reduced graphene oxide composite with enhanced electrochemical supercapacitance performance. *Bull. Chem. Soc. Jpn.* **2017**, *90*, 955–962. [[CrossRef](#)]
18. Zhang, K.; Ying, G.; Liu, L.; Ma, F.; Su, L.; Zhang, C.; Wu, D.; Wang, X.; Zhou, Y. Three-dimensional porous Ti<sub>3</sub>C<sub>2</sub>Tx-NiO composite electrodes with enhanced electrochemical performance for supercapacitors. *Materials* **2019**, *12*, 188. [[CrossRef](#)]
19. Zhou, M.; Liang, R.; Zhou, Z.; Dong, X. Novel BaTiO<sub>3</sub>-based lead-free ceramic capacitors featuring high energy storage density, high power density and excellent stability. *J. Mater. Chem. C* **2018**, *6*, 8528–8537. [[CrossRef](#)]
20. Hu, P.; Sun, W.; Fan, M.; Qian, J.; Jiang, J.; Dan, Z.; Lin, Y.; Nan, C.W.; Li, M.; Shen, Y. Large energy density at high-temperature and excellent thermal stability in polyimide nanocomposite contained with small loading of BaTiO<sub>3</sub> nanofibers. *Appl. Surf. Sci.* **2018**, *458*, 743–750. [[CrossRef](#)]
21. Wang, B.; Ma, Y.; Na, B.; Lv, R.; Liu, H.; Li, W.; Zhou, H. Enhanced dielectric thermal stability and permittivity of flexible composite films based on BaTiO<sub>3</sub> nanoparticles highly filled PVDF/PAN blend nanofibrous membranes. *Polym. Compos.* **2018**, *39*, E1841–E1848. [[CrossRef](#)]
22. Bi, M.; Hao, Y.; Zhang, J.; Lei, M.; Bi, K. Particle size effect of BaTiO<sub>3</sub> nanofillers on the energy storage performance of polymer nanocomposites. *Nanoscale* **2017**, *9*, 16386–16395. [[CrossRef](#)] [[PubMed](#)]
23. Yao, L.; Pan, Z.; Zhai, J.; Zhang, G.; Liu, Z.; Liu, Y. High-energy-density with polymer nanocomposites containing of SrTiO<sub>3</sub> nanofibers for capacitor application. *Compos. Part A Appl. Sci. Manuf.* **2018**, *109*, 48–54. [[CrossRef](#)]
24. Guan, S.; Li, H.; Zhao, S.; Guo, L. The surface modification of BaTiO<sub>3</sub> and its effects on the microstructure and electrical properties of BaTiO<sub>3</sub>/silicone rubber composites. *J. Vinyl Addit. Technol.* **2018**, *24*, 288–294. [[CrossRef](#)]
25. Luo, S.; Shen, Y.; Yu, S.; Wan, Y.; Liao, W.H.; Sun, R.; Wong, C.P. Construction of a 3D-BaTiO<sub>3</sub> network leading to significantly enhanced dielectric permittivity and energy storage density of polymer composites. *Energy Environ. Sci.* **2017**, *10*, 137–144. [[CrossRef](#)]

26. Airimioaei, M.; Buscaglia, M.T.; Tredici, I.; Anselmi-Tamburini, U.; Ciomaga, C.E.; Curecheriu, L.; Bencan, A.; Buscaglia, V.; Mitoseriu, L. SrTiO<sub>3</sub>-BaTiO<sub>3</sub> nanocomposites with temperature independent permittivity and linear tunability fabricated using field-assisted sintering from chemically synthesized powders. *J. Mater. Chem. C* **2017**, *5*, 9028–9036. [[CrossRef](#)]
27. Hu, P.; Gao, S.; Zhang, Y.; Zhang, L.; Wang, C. Surface modified BaTiO<sub>3</sub> nanoparticles by titanate coupling agent induce significantly enhanced breakdown strength and larger energy density in PVDF nanocomposite. *Compos. Sci. Technol.* **2018**, *156*, 109–116. [[CrossRef](#)]
28. Chen, S.; Lv, X.; Han, X.; Luo, H.; Bowen, C.R.; Zhang, D. Significantly improved energy density of BaTiO<sub>3</sub> nanocomposites by accurate interfacial tailoring using a novel rigid-fluoro-polymer. *Polym. Chem.* **2018**, *9*, 548–557. [[CrossRef](#)]
29. Xie, Y.; Jiang, W.; Fu, T.; Liu, J.; Zhang, Z.; Wang, S. Achieving high energy density and low loss in PVDF/BST nanodielectrics with enhanced structural homogeneity. *ACS Appl. Mater. Interfaces* **2018**, *10*, 29038–29047. [[CrossRef](#)]
30. Fu, J.; Hou, Y.; Zheng, M.; Zhu, M. Comparative study of dielectric properties of the PVDF composites filled with spherical and rod-like BaTiO<sub>3</sub> derived by molten salt synthesis method. *J. Mater. Sci.* **2018**, *53*, 7233–7248. [[CrossRef](#)]
31. Zhu, P.; Sun, R.; Wong, C. Facile Synthesis of BaTiO<sub>3</sub> Nanorods and Their Shape Effects on the Dielectric Constants of Polymer Composites. In Proceedings of the IEEE 63rd Electronic Components and Technology Conference, Las Vegas, NV, USA, 28–31 May 2013; pp. 1071–1075.
32. Gao, J.; Shi, H.; Dong, H.; Zhang, R.; Chen, D. Factors influencing formation of highly dispersed BaTiO<sub>3</sub> nanospheres with uniform sizes in static hydrothermal synthesis. *J. Nanopart. Res.* **2015**, *17*, 286. [[CrossRef](#)]
33. Zhang, K.; Gao, F.; Xu, J.; Wang, L.; Zhang, Q.; Kong, J. Fabrication and dielectric properties of Ba<sub>0.6</sub>Sr<sub>0.4</sub>TiO<sub>3</sub>/acrylonitrile-butadiene-styrene resin composites. *J. Mater. Sci. Mater. Electron.* **2017**, *28*, 8960–8968. [[CrossRef](#)]
34. Nootsuwan, N.; Plungpongpan, K.; Wattanathana, W.; Koonsaeng, N.; Laobuthee, A.; Manuspiya, H. Dielectric and mechanical properties of poly(butylene succinate) thin film composites incorporated with barium strontium titanate powder. *Integr. Ferroelectr.* **2016**, *174*, 155–166. [[CrossRef](#)]
35. Chi, Q.; Gao, Z.; Zhang, C.; Cui, Y.; Dong, J.; Wang, X.; Lei, Q. Dielectric properties of sandwich-structured BaTiO<sub>3</sub>/polyimide hybrid films. *J. Mater. Sci. - Mater. Electron.* **2017**, *28*, 15142–15148. [[CrossRef](#)]
36. Xie, Y.; Wang, J.; Yu, Y.; Jiang, W.; Zhang, Z. Enhancing breakdown strength and energy storage performance of PVDF-based nanocomposites by adding exfoliated boron nitride. *Appl. Surf. Sci.* **2018**, *440*, 1150–1158. [[CrossRef](#)]
37. Dai, Y.; Zhu, X. Improved dielectric properties and energy density of PVDF composites using PVP engineered BaTiO<sub>3</sub> nanoparticles. *Korean J. Chem. Eng.* **2018**, *35*, 1570–1576. [[CrossRef](#)]
38. He, D.; Wang, Y.; Chen, X.; Deng, Y. Core-shell structured BaTiO<sub>3</sub>@Al<sub>2</sub>O<sub>3</sub> nanoparticles in polymer composites for dielectric loss suppression and breakdown strength enhancement. *Compos. Part A Appl. Sci. Manuf.* **2017**, *93*, 137–143. [[CrossRef](#)]
39. Huang, Q.; Luo, H.; Chen, C.; Zhou, K.; Zhang, D. Improved energy density and dielectric properties of P(VDF-HFP) composites with TiO<sub>2</sub> nanowire clusters. *J. Electroceram.* **2018**, *40*, 65–71. [[CrossRef](#)]
40. Huang, Q.; Luo, H.; Chen, C.; Zhou, X.; Zhou, K.; Zhang, D. Enhanced energy density in P(VDF-HFP) nanocomposites with gradient dielectric fillers and interfacial polarization. *J. Alloys Compd.* **2017**, *696*, 1220–1227. [[CrossRef](#)]
41. Wang, J.; Long, Y.; Sun, Y.; Zhang, X.; Yang, H.; Lin, B. Enhanced energy density and thermostability in polyimide nanocomposites containing core-shell structured BaTiO<sub>3</sub>@SiO<sub>2</sub> nanofibers. *Appl. Surf. Sci.* **2017**, *426*, 437–445. [[CrossRef](#)]
42. Zheng, M.S.; Zheng, Y.T.; Zha, J.W.; Yang, Y.; Han, P.; Wen, Y.Q.; Dang, Z.M. Improved dielectric, tensile and energy storage properties of surface rubberized BaTiO<sub>3</sub>/polypropylene nanocomposites. *Nano Energy* **2018**, *48*, 144–151. [[CrossRef](#)]
43. Wang, J.; Long, Y.; Sun, Y.; Zhang, X.; Yang, H.; Lin, B. Fabrication and enhanced dielectric properties of polyimide matrix composites with core-shell structured CaCu<sub>3</sub>Ti<sub>4</sub>O<sub>12</sub>@TiO<sub>2</sub> nanofibers. *J. Mater. Sci. Mater. Electron.* **2018**, *29*, 7842–7850. [[CrossRef](#)]
44. Wang, Y.; Wu, X.; Feng, C.; Zeng, Q. Improved dielectric properties of surface modified BaTiO<sub>3</sub>/polyimide composite films. *Microelectron. Eng.* **2016**, *154*, 17–21. [[CrossRef](#)]



© 2019 by the authors. Licensee MDPI, Basel, Switzerland. This article is an open access article distributed under the terms and conditions of the Creative Commons Attribution (CC BY) license (<http://creativecommons.org/licenses/by/4.0/>).